

X-ray fluorescent lines from the Compton-thick AGN in M51

Weiwei Xu, Zhu Liu, Lijun Gou, and Jiren Liu

National Astronomical Observatories, 20A Datun Road, Beijing 100012, China; weiweixu@nao.cas.cn, jirenliu@nao.cas.cn

ABSTRACT

The cold disk/torus gas surrounding active galactic nuclei (AGN) emits fluorescent lines when irradiated by hard X-ray photons. The fluorescent lines of elements other than Fe and Ni are rarely detected due to their relative faintness. We report the detection of $K\alpha$ lines of neutral Si, S, Ar, Ca, Cr, and Mn, along with the prominent Fe $K\alpha$, Fe $K\beta$, and Ni $K\alpha$ lines, from the deep *Chandra* observation of the low-luminosity Compton-thick AGN in M51. The Si $K\alpha$ line at 1.74 keV is detected at $\sim 3\sigma$, the other fluorescent lines have a significance between 2 and 2.5σ , while the Cr line has a significance of $\sim 1.5\sigma$. These faint fluorescent lines are made observable due to the heavy obscuration of the intrinsic spectrum of M51, which is revealed by *NuSTAR* observation above 10 keV. The hard X-ray continuum of M51 from *Chandra* and *NuSTAR* can be fitted with a power-law spectrum with an index of 1.8, reprocessed by a torus with an equatorial column density of $N_{\text{H}} \sim 7 \times 10^{24} \text{ cm}^{-2}$ and an inclination angle of 74 degrees. This confirms the Compton-thick nature of the nucleus of M51. The relative element abundances inferred from the fluxes of the fluorescent lines are similar to their solar values, except for Mn, which is about 10 times overabundant. It indicates that Mn is likely enhanced by the nuclear spallation of Fe.

Key words: atomic processes – galaxies: Seyfert – galaxies: individual: M51 (NGC 5194) – X-rays: galaxies

1 INTRODUCTION

The majority of nearby active galactic nuclei (AGN) are obscured by large amounts of cold gas and dust (e.g. Comastri 2004). For Compton thick AGN with absorption column densities larger than $1.5 \times 10^{24} \text{ cm}^{-2}$ (the inverse of the Thomson cross-section), the continuum below 10 keV is heavily suppressed, and Compton scattering of high energy photons produces a spectral bump around 20 – 30 keV. The cold gas emits fluorescent lines when irradiated by the central AGN. The most prominent line is the Fe $K\alpha$ line at 6.4 keV, due to its high abundance and high fluorescence yield. The Fe 6.4 keV line is found to be a ubiquitous feature of AGN (e.g. Shu et al. 2010, and reference therein). Since the continuum is heavily suppressed for Compton-thick AGN, their Fe 6.4 keV line will be more noticeable. Indeed, the Fe 6.4 keV lines with equivalent width (EW) as large as a few keV have been reported (e.g. Levenson et al. 2002).

For those AGN with noticeable Fe $K\alpha$ lines, the fluorescent lines from elements other than Fe should also be detectable. The fluorescent lines of other elements are generally thought to be observationally irrelevant, due to their small yields. Nevertheless, the yields of other elements are not as small as unobservable. For example, the yield of neutral Si $K\alpha$ is 0.042, larger than 10% of that of the neutral Fe $K\alpha$. The fluxes of the fluorescent lines are determined by the chemical abundances, the distribution of the obscuring material, as well as the illuminating intrinsic spectrum of AGN.

If detected, the non-Fe fluorescent lines can be used to measure the abundances of the cold gas. A possible example is the *ASCA* observation of NGC 6552 that shows $K\alpha$ lines of seven neutral species, which were used to constrain the abundances of the cold gas (Fukazawa et al. 1994; Reynolds et al. 1994).

In this letter we report the detection of fluorescent lines of neutral Si, S, Ar, Ca, Cr, and Mn, along with the prominent Fe $K\alpha$, Fe $K\beta$, and Ni $K\alpha$ lines, from the deep *Chandra* spectrum of the nucleus of M51 (NGC 5194). Known as the Whirlpool galaxy, M51 is classified as a LINER/Seyfert II galaxy (e.g. Stauffer 1982; Ho et al. 1997). Its face-on inclination and close distance (7.1 Mpc, Takáts & Vinkó 2001) allow detailed studies of the nuclear activity (see e.g. Liu & Mao 2015, and references therein). While the X-ray luminosity of the nucleus of M51 in 2 – 10 keV band is as low as $\sim 10^{39} \text{ erg s}^{-1}$, the EW of the Fe 6.4 keV line is $\sim 4 \text{ keV}$, the largest one ever reported (e.g. Terashima & Wilson 2001; Levenson et al. 2002). Such a large EW implies a column density larger than $3 \times 10^{24} \text{ cm}^{-2}$ as shown by Monte-Carlo simulations of Compton-thick torus (Ikeda et al. 2009; Murphy & Yaqoob 2009).

A bright hard X-ray excess above 10 keV had been reported from the *BeppoSAX* observation of M51 (Fukazawa et al. 2001), and an absorption column density $\sim 10^{24} \text{ cm}^{-2}$ was inferred. The lack of spatial information of *BeppoSAX*, however, makes the inference uncertain. Indeed, as shown in §2, the *NuSTAR* observation of M51 detects at least three sources within its field of view (FOV).

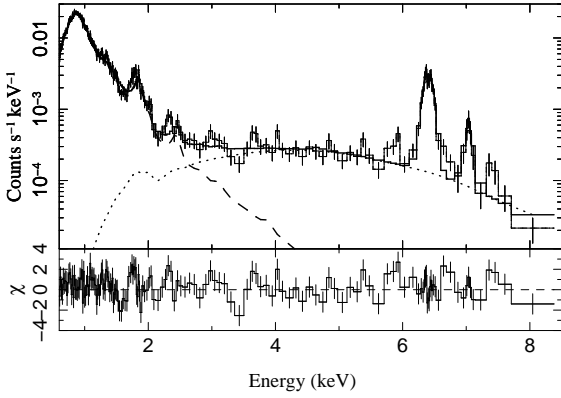


Figure 2. *Chandra* spectrum of the nucleus of M51 merged from all twelve datasets. The fitted model of Vapec (dashed line) plus a powerlaw (dotted line) and two Gaussians is over-plotted. Many residual peaks are around the energies of $K\alpha$ lines of neutral species.

We include the *NuSTAR* data of the nucleus of M51 to constrain the continuum above 10 keV.

2 OBSERVATIONAL DATA

The half-arcsec spatial resolution of *Chandra* makes it possible to resolve the point sources in the nuclear region of M51. This helps to reduce the contamination of other sources to the nucleus of M51. We use twelve *Chandra* archival observations with ObsID numbers of 13812, 13813, 13814, 13815, 13816, 15496, 15553, 1622, 354, 3932, 12562, and 12668, all of which were taken with ACIS-S. The datasets are analyzed with *CIAO* (version 4.6) following standard procedures. After removing the flare periods, the total effective exposure time is about 800 ks, and the total count number is about 12,000 for the nucleus. All datasets are aligned to each other using the *CIAO* tools of *wcs_match* and *wcs_update*. As an illustration, the counts image of M51 within 2 – 7.5 keV band merged from all datasets is plotted in the left panel of Figure 1. It is dominated by an off-nuclear ULX. While the nucleus is relatively faint within 2 – 7.5 keV band, its striking 6.4 keV line (as shown in Figure 2) indicates the hidden AGN. The extended emission can be clearly seen in Figure 1, which has been studied previously (e.g. Owen & Warwick 2009).

M51 was observed with *NuSTAR* for a short exposure of 18.5 ks on Oct. 2012. The data is reduced using NUSTARDAS software and the effective exposure is about 15 ks after cleaning. In the right panel of Figure 1, we show the *NuSTAR* image of M51 combining the two focal plane modules of FPMA and FPMB. Besides the nucleus, there are two other sources detected by *NuSTAR* (indicated as black crosses in Figure 1), which correspond to sources 69 (upper one) and 82 (lower-left one) as in Terashima & Wilson (2004).

3 RESULTS

The spectrum of the nucleus of M51 is extracted from a 2'' radius for each *Chandra* observation with a background spectrum extracted from a source-free region. We compared the spectra of different observations and found no apparent variability. Thus we combine them using the ISIS function *combine_datasets*, for which the model is calculated for each dataset, and the datasets

Table 1. Model of MYTorus+Vapec+Gaussians fitted to the spectra of the nucleus of M51

MYTorus+Vapec	Value
Intrinsic powerlaw index, Γ	1.8 ± 0.3
Intrinsic powerlaw normalization	0.002 ± 0.0015
MYTorus equatorial column density (10^{24} cm^{-2}) ^a	7.0 ± 3.0
MYTorus inclination angle (degrees)	74 ± 8
Absorption column density of Vapec (10^{22} cm^{-2})	0.05 ± 0.04
Vapec temperature (keV)	0.74 ± 0.03
Vapec normalization (10^{-5})	7.1 ± 1.4
Vapec O	0.3 ± 0.3
Vapec Ne	0.5 ± 0.3
Vapec Mg, Al	0.2 ± 0.1
Vapec Si, S, Ar, Ca	0.3 ± 0.1
Vapec Fe, Ni	0.2 ± 0.1
$\chi^2/d.o.f.$	169.3/155 ~ 1.1

Line	Energy(keV)	Flux	Y_x	Z_x/Z_{Fe}	$\Delta\chi^{2b}$	Sig. ^c
Si $K\alpha$	1.74	1.9 ± 0.8	0.042	0.8 ± 0.3	16.0	99.6%
S $K\alpha$	2.31	1.3 ± 0.7	0.078	0.6 ± 0.3	8.3	97.4%
Ar $K\alpha$	2.96	0.8 ± 0.5	0.112	0.9 ± 0.6	6.2	97.0%
Ca $K\alpha$	3.69	0.9 ± 0.5	0.124	1.3 ± 0.7	8.7	97.5%
Cr $K\alpha$	5.41	0.7 ± 0.6	0.25	2.2 ± 1.9	2.4	85.8%
Mn $K\alpha$	5.89	1.8 ± 0.9	0.278	9.8 ± 4.9	8.8	97.7%
Fe $K\alpha$	6.40 ± 0.01	38.0 ± 3.3	0.304	1	–	–
Ni $K\alpha$	7.42 ± 0.04	4.4 ± 2.2	0.37	2.2 ± 1.1	10.2	98.3%
Fe $K\beta$	7.03 ± 0.02	7.8 ± 2.2	–	–	–	–
Fe XXV $K\alpha$	6.7	1.8 ± 1.3	–	–	5.3	96.5%

Note: The abundances of Vapec are relative to their solar values. All the line energies are fixed at expected values, except for Fe $K\alpha$, Fe $K\beta$, and Ni $K\alpha$, which are fitted. The line flux is in units of 10^{-7} photons $\text{cm}^{-2} \text{ s}^{-1}$. The yield Y_x is taken from Kaastra & Mewe (1993). The errors quoted are for 90% confidence level. ^aThe upper limit of the equatorial column density is beyond the valid N_{H} value of MYTorus model of 10^{25} cm^{-2} . ^b $\Delta\chi^2$ is the improvement of χ^2 by adding the line. ^cThe significance is estimated based on Monte-Carlo simulations.

and models are summed separately before computing the χ^2 (Houck & Denicola 2000). The combined spectrum is plotted in Figure 2, which is binned to a minimum signal-to-noise (S/N) ratio of 4.5 below 6.8 keV and 3 above that to enhance the visibility of emission lines of low counts. We see that the spectrum has a significant soft component below 2 keV, which is likely due to the shock-heated gas by the radio jet (Terashima & Wilson 2001). While above 2 keV, the most prominent feature are the emission lines at 6.4 and 7 keV, which are the $K\alpha$ and $K\beta$ lines of neutral-like Fe. In addition, there are also many emission spikes between 2 and 6 keV.

We first try to fit the *Chandra* spectrum of M51 with a thermal model (Vapec, Foster et al. 2012), representing the soft component, plus an absorbed powerlaw model for the hard component. We include two Gaussians to represent the Fe $K\alpha$ and $K\beta$ lines. The fitted result is plotted in Figure 2. The fitted temperature of the thermal component is about 0.7 keV, a little higher than the value reported by Terashima & Wilson (2001). The fitted powerlaw index is about -0.3, implying a heavily reprocessed continuum. In the residual panel of Figure 2, there are many remaining spikes, such as the ones around 1.7 keV, 2.3 keV, 5.9 keV, and 7.5 keV. We find they are exactly corresponding to the $K\alpha$ emission lines of neutral Si, S, Mn, and Ni. Therefore, they are most likely due to the fluorescent lines of neutral species as the Fe 6.4 keV line.

To measure the observed line fluxes, it is better to use a

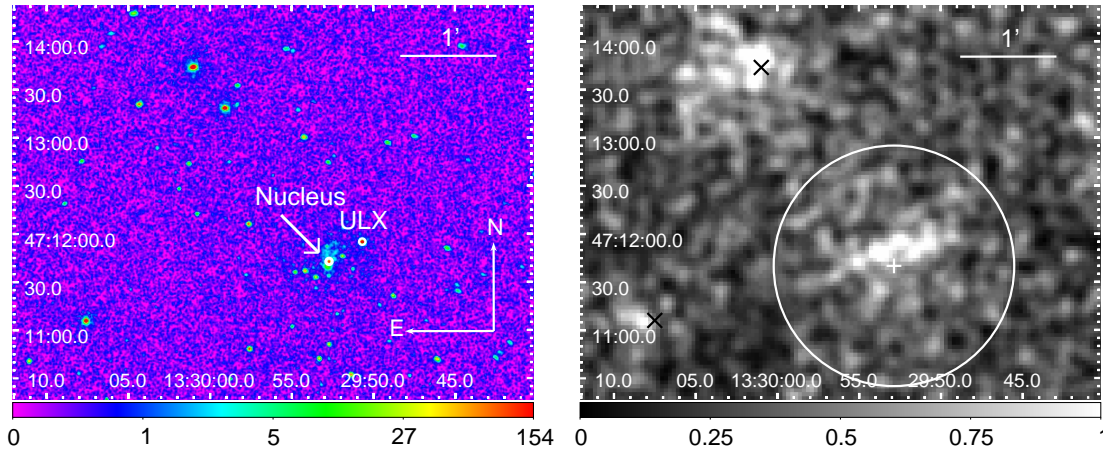


Figure 1. Left: *Chandra* image of M51 within 2 – 7.5 keV band merged from all twelve datasets. The nuclear emission is dominated by a ULX 25'' away from the nucleus. Right: *NuSTAR* image of M51 combining both FPMA and FPMB data. The white plus sign marks the nucleus of M51, and the circle with a radius of 75'' indicates the spectral extraction region. The two black crosses indicate the other two sources detected by *NuSTAR*. The *Chandra* and *NuSTAR* images are smoothed with a Gaussian of 2 (1'') and 3 (7.4'') pixels, respectively.

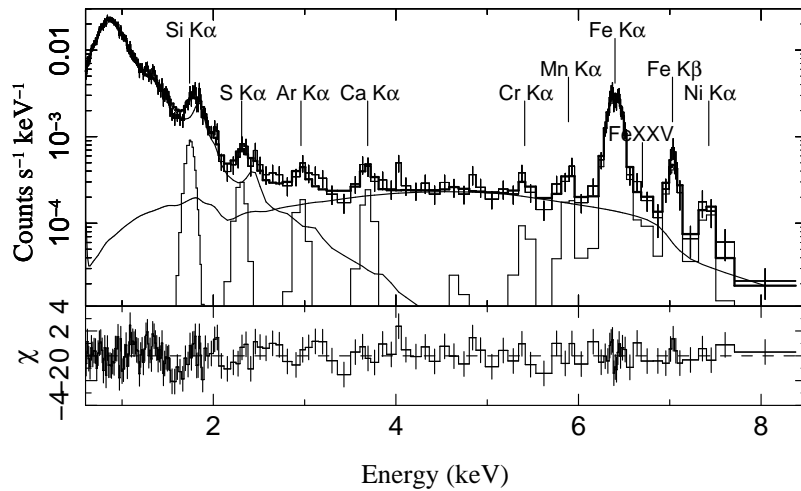


Figure 3. The model of Vapex+MYTorus+Gaussians fitted to the *Chandra* spectrum of the nucleus of M51. Each component is overlaid individually. The residuals around the added $K\alpha$ lines are reduced significantly. The model line feature around 4.6 keV is the instrumental Si escape peak, which follows the Fe 6.4 keV line and is about 1% of the intensity of the Fe line (Grimm et al. 2009).

scattered continuum rather than a powerlaw. For this purpose, we adopt the MYTorus model (Murphy & Yaqoob 2009; Yaqoob 2012), which is based on Monte-Carlo simulations of a toroidal geometry. The MYTorus model is specified by the incident powerlaw continuum, the equatorial column density, and the inclination angle. It provides separable components of transmitted continuum, scattered continuum, and the Fe $K\alpha$ and $K\beta$ fluorescent lines for a solar abundance (Anders & Grevesse 1989). Fluorescent lines from other elements are not included. Thus we replace the powerlaw model with the MYTorus continuum, which includes the transmitted and scattered components. We then add Gaussian lines centred at the energies of the $K\alpha$ lines of neutral elements, including Si, S, Ar, Ca, Cr, Mn, and Ni. We also add a Gaussian line at 6.7 keV, where seems to be a faint Fe XXV $K\alpha$ line.

To further constrain the continuum model of MYTorus, we include the *NuSTAR* spectrum of M51 into the fitting, which is ex-

tracted from a circle region of 75'' radius as indicated in Figure 1. The background spectrum is extracted from a source-free region. The spectra of FPMA and FPMB are combined using ISIS function *combine_datasets*. Because *NuSTAR* has a half-power diameter of 58'', its spectrum of the nucleus of M51 is contaminated by neighbouring sources. The dominate one is the ULX as indicated in the left panel of Figure 1, the *Chandra* spectrum (2.3–7 keV) of which can be well fitted with an absorbed powerlaw with a photon index of 1.85 and a column density of $6.5 \times 10^{22} \text{ cm}^{-2}$. We also extract a spectrum from a circle region of 60'' radius excluding the nucleus and the ULX, which can be fitted with a powerlaw with an index of 2.4 without absorption. The region of 60'' radius includes most of the extended emission and point sources that contaminate the *NuSTAR* spectrum. Therefore, besides the model for the nucleus of *Chandra* data, we also assign these two powerlaw models with

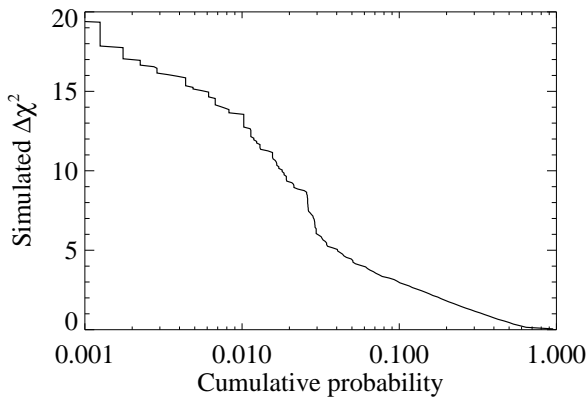


Figure 4. Distribution of the improvement of χ^2 for the addition of an emission line for simulated fake spectra of a null hypothesis model including Vapex, a continuum, and only Fe $K\alpha$ and $K\beta$ lines.

fixed parameters to the *NuSTAR* data. The instrument normalization between *Chandra* and *NuSTAR* is fixed.

The fitting results are listed in Table 1 and plotted in Figure 3 for the *Chandra* data. We see that the model provides a reasonable fit to the observed spectrum. The improvement of χ^2 with the addition of each line is also listed in Table 1. There is a residual spike around 4.02 keV, which could be due to the fluorescent lines of Ca $K\beta$ (4.01 keV), Sc $K\alpha$ (4.09 keV), and/or Ca xx $Ly\alpha$ line (4.11 keV). If it is the Ca $K\beta$ line, the measured Ca $K\alpha$ /Ca $K\beta$ ratio (~ 1.5) would be too small compared with the expected value of 10 (Kaastra & Mewe 1993). Since it is relatively weak ($\Delta\chi^2 \sim 4$ adding two parameters) and offset from the expected fluorescent energies, we neglected it here. The residuals below 2 keV are likely due to the simple model of one thermal component. The fitted equatorial column density of the MYTorus model is $\sim 7 \times 10^{24} \text{ cm}^{-2}$, close to the up-limit of the valid column density of MYTorus. It confirms the Compton-thick nature of the nucleus of M51. The fitted intrinsic powerlaw index is 1.8, typical of unobscured AGN. The model luminosity within 2 – 10 keV is $6.7 \times 10^{38} \text{ erg s}^{-1}$, while the intrinsic luminosity corrected for the absorption is $4 \times 10^{40} \text{ erg s}^{-1}$. The best fitted EW of the Fe $K\alpha$ and Fe $K\beta$ lines are 4.1 and 1.2 keV, respectively.

To estimate the significance of the detection of each line, we use the Monte-Carlo method following Markowitz et al. (2006). We generate 1000 fake spectra using the exposures and responses of the *Chandra* observations for a null hypothesis model including Vapex, a continuum, and only the Fe $K\alpha$ and $K\beta$ lines. For simplicity, we adopt the powerlaw continuum model in Figure 2, instead of the continuum model of MYTorus, both of which are similar in 2 – 8 keV band. We then calculate the improvement of χ^2 over the null hypothesis model by adding an emission line around the energy of each detected line (within a range of ± 0.1 keV). The cumulative distribution of the $\Delta\chi^2$ is created for each line. We find the distributions are similar for different lines except the one of Ni line for $\Delta\chi^2 < 5$. Therefore we adopt an $\Delta\chi^2$ distribution averaged over all lines, which is plotted in Figure 4. The estimated significance of the detection of each line is listed in the last column of Table 1. We see that the Si line is detected at $\sim 3\sigma$, and the other fluorescent lines have a significance between 2 and 2.5σ , while the Cr line has a significance of $\sim 1.5\sigma$.

The unfolded spectrum for *NuSTAR* data is plotted in Figure 5. There are totally about 1200 photons in the *NuSTAR* spectra and

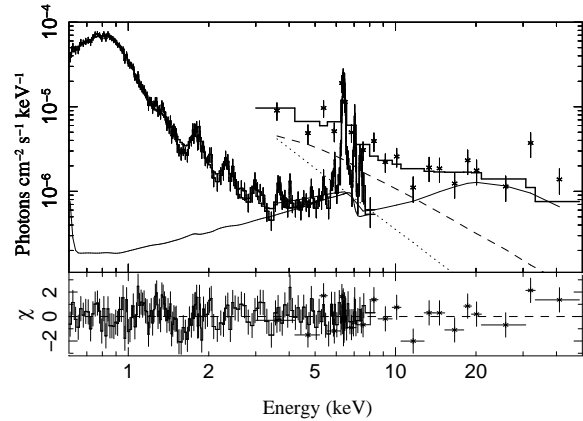


Figure 5. The unfolded *NuSTAR* spectrum of M51 (cross points) along with the fitted results (thick histogram). The continuum model of MYTorus (solid line) is over-plotted, together with the contaminating powerlaw models of the ULX (dashed line) and the nuclear region excluding the nucleus and the ULX (dotted line). Below ~ 10 keV, the *NuSTAR* spectrum is dominated by the ULX, while above that it is dominated by the nucleus. For comparison, the *Chandra* spectrum and its unfolded MYTorus model are also plotted.

only the 3 – 50 keV energy range is used due to the low S/N of the data above 50 keV. We see that below ~ 10 keV the spectrum is dominated by the ULX indicated in Figure 1, while above that the nucleus dominates. Because the exposure of the *NuSTAR* observation is short, there are no many photons above 20 keV and the intrinsic spectrum is not well constrained. Further deep *NuSTAR* observations will help to determine the intrinsic spectrum.

To estimate the Fe abundance, we replace the two Gaussian lines of Fe $K\alpha$ and Fe $K\beta$ with the component of Fe fluorescent lines of MYTorus model and allow its normalization to vary. We find that the normalization of the line component of MYTorus is about 2 times that of the continuum component. Nevertheless, it does not necessarily mean Fe is overabundant. Gohil & Ballantyne (2015) showed that the EW of the Fe $K\alpha$ line could be enhanced by dust due to the reduction of the reflected continuum intensity caused by the smaller backscattering opacity of dust. This dust effect needs to be investigated to obtain the Fe abundance.

4 DISCUSSION

The Compton-thick nature of the nucleus of M51 is confirmed by the *NuSTAR* observation of hard X-ray emission above 10 keV. The fitted equatorial column density of MYTorus model is $\sim 7 \times 10^{24} \text{ cm}^{-2}$. This value is consistent with the detection of strong HCN emission at the nucleus of M51, which suggests the presence of compact dense molecular gas (Matsushita et al. 2015). A gas disk/torus with a density of $\sim 10^6 \text{ cm}^{-3}$ and a pc-scale size can provide the fitted column density.

We detected the faint fluorescent lines of neutral Si, S, Ar, Ca, Cr, and Mn, along with the prominent Fe $K\alpha$, Fe $K\beta$, and Ni $K\alpha$ lines, from the deep *Chandra* observation of M51. These lines can be used to measure their abundances. As the reprocessing matter is Compton-thick, detailed radiative calculations, such as those by Murphy & Yaqoob (2009), are needed to obtain accurate results. Nevertheless, the relative abundance can be roughly estimated as follows.

The observed fluorescent lines are most likely due to the scattering from a surface layer of unit optical depth that is not heavily absorbed by the torus itself. The fluorescence flux of certain element x can be expressed as follows (e.g. George & Fabian 1991)

$$F_x \propto Y_x \int_{E_x}^{\infty} AE^{-\Gamma} \frac{Z_x \sigma_{x,k}(E)}{\sigma_T(E)} dE, \quad (1)$$

where Y_x is the fluorescence yield, $AE^{-\Gamma}$ is the incident photon spectrum, Z_x is the abundance relative to solar value, and $\sigma_{x,k}$ and σ_T are the absorption cross-sections of the K-shell electron of element x and of all elements, respectively. $\frac{Z_x \sigma_{x,k}}{\sigma_T}$ expresses the probability that a photon is absorbed by the K-shell electron of element x . For $Z_{Fe} > 1$, Fe dominates the opacity above the binding energy of Fe and σ_T is sensitive to Z_{Fe} . This dependence is neglected for the rough estimate here. We also neglect the difference of the absorption of produced fluorescent photons.

The estimated abundances relative to Fe are listed in Table 1. The α elements of Si, S, Ca, and Ar have an abundance pattern similar to that of the Sun. While for the trace element of Mn, its abundance is about 10 times overabundant. This enhancement of Mn is likely due to the nuclear spallation of Fe caused by cosmic rays from the nucleus (Skibo 1997; Turner & Miller 2010). In principle, it is possible that the soft Vapex component is due to the jet-heated gas, which originally is part of the disk/torus gas emitting fluorescent lines. In this case, the abundances of the Vapex model should be similar to those estimated from the fluorescent lines. The relative abundance of Si, S, Ca, and Ar to Fe is about 1.5 for the Vapex model, a little higher than those estimated from the fluorescent lines. This is expected since lower energy photons have a larger probability of being absorbed than higher energy photons. Nevertheless, the details of the absorption depend on the distribution of the obscuring material and further modelling is needed for rigorous comparison. These results show that the non-Fe fluorescent lines can be a valuable probe of the obscuring matter of AGN and the physical processes they related to.

As noted in §1, the EW of the Fe 6.4 keV line of M51 is as large as 4 keV. This large EW of the Fe line is due to the suppression of the illuminating intrinsic spectrum, which also makes it possible to detect non-Fe fluorescent lines much fainter than the Fe line. In fact, M51 is the only one with an EW of the Fe line larger than 2.5 keV in Levenson et al. (2002). It would be difficult to detect non-Fe fluorescent lines for samples with lower EW of the Fe line. A search with other Compton-thick samples with an EW of the Fe line $\sim 1 - 2$ keV is undertaking.

ACKNOWLEDGEMENTS

We thank our referee for valuable comments. JL is supported by NSFC grant 11203032, and LG is supported by the Strategic Priority Research Program ‘‘The Emergence of Cosmological Structures’’ of CAS grant XDB09000000, NSFC grant 11333005, and NAOC grant Y234031001. This research is based on data obtained from the *Chandra* Data Archive and uses data from *NuSTAR* mission.

REFERENCES

- Anders, E. & Grevesse, N. 1989, *Geochimica et Cosmochimica Acta*, 53, 197
Comastri, A. 2004, *ASSL*, 308, 245

- Foster, A. R., Ji, L., Smith, R. K. and Brickhouse, N. S. 2012, *ApJ*, 756, 128
Fukazawa, Y., Iyomoto, N., Kubota, A., Matsumoto, Y., Makishima, K. 2001, *A&A*, 374, 73
Fukazawa, Y., Makishima, K., Ebisawa, K., Fabian, A. C., Gendreau, K. C., Ikebe, Y., Iwasawa, K., Kii, T. et al. 1994, *PASJ*, 46, 141
George, I. M. & Fabian, A. C. 1991, *MNRAS*, 249, 352
Grimm, H. J., McDowell, J., Fabbiano, G., Elvis, M. 2009, *ApJ*, 690, 128
Gohil, R. & Ballantyne, D. R. 2015, *MNRAS*, 449, 1449
Ho, L. C., Filippenko, A. V., Sargent, W. L. W. 1997, *ApJS*, 112, 315
Houck, J. C. & Denicola, L. A. 2000, in *Astronomical Data Analysis Software and Systems IX*, eds. Manset, N., Veillet, C., & Crabtree, D. ASP Conf. Ser., 216, 591
Ikeda, S., Awaki, H., Terashima, Y. 2009, *ApJ*, 692, 608
Kaastra, J. S. & Mewe, R. 1993, *A&AS*, 97, 443
Liu, J. & Mao, S. 2015, preprint (astro-ph/1505.07175)
Levenson, N. A., Krolik, J. H., Zycki, P. T., Heckman, T. M., Weaver, K. A., Awaki, H., Terashima, Y. 2002, *ApJL*, 573, 81
Markowitz, A., Reeves, J. N., Braito, V. 2006, *ApJ*, 646, 783
Matsushita, S., Trung, D., Boone, F., Krips, M., Lim, J., Muller, S. 2015, *ApJ*, 799, 26
Murphy, K. D. & Yaqoob, T. 2009, *MNRAS*, 397, 1549
Owen, R. A. & Warwick, R. S. 2009, *MNRAS*, 394, 1741
Palmeri, P., Mendoza, C., Kallman, T. R., Bautista, M. A., Mendenhall, M. 2003, *A&A*, 410, 359
Reynolds, C. S., Fabian, A. C., Makishima, K., Fukazawa, Y., Tamura, T. 1994, *MNRAS*, 268L, 55
Shu, X. W., Yaqoob, T., Wang, J. X. 2010, *ApJS*, 187, 581
Skibo, J. G. 1997, *ApJ*, 478, 522
Stauffer, J. R. 1982, *ApJS*, 50, 517
Takáts, K. & Vinkó, J. 2006, *MNRAS*, 372, 1735
Terashima, Y. & Wilson, A. S. 2001, *ApJ*, 560, 139
Terashima, Y. & Wilson, A. S. 2004, *ApJ*, 601, 735
Turner, T. J. & Miller, L. 2010, *ApJ*, 709, 1230
Yaqoob, T. 2012, *MNRAS*, 423, 3360